**Harvey Williams**[1]
Schlumberger Gould Research,
High Cross, Madingley Road,
Cambridge CB3 0EL, UK
e-mail: HW35711@outlook.com

**Michael McPhail**
Mathematical Institute,
University of Oxford,
Oxford OX2 6GG, UK
e-mail: michael.mcphail@maths.ox.ac.uk

**Sourav Mondal**
Mathematical Institute,
University of Oxford,
Oxford OX2 6GG, UK
e-mail: souravmondal2008@gmail.com

**Andreas Münch**
Mathematical Institute,
University of Oxford,
Oxford OX2 6GG, UK
e-mail: muench@maths.ox.ac.uk

# Modeling Gel Fiber Formation in an Emerging Coaxial Flow From a Nozzle

*It is important to understand the operational aspects which affect the continuous fabrication of alginate gel fibers. These can be formed from a cross-linking reaction of an alginate precursor injected into a coaxial annular pipe flow with a calcium chloride solution. This is an example of an emerging solid interface that interacts with the flow in its neighborhood. We advance on earlier works by relaxing assumptions of a fixed spatial domain to explore and observe mechanisms controlling gel radius. We use two different models. The first one represents the gel layer as a capillary interface between two immiscible liquids and captures the effect of surface tension. A second model is introduced to treat the cross-linking chemical reaction and its effect on the viscosity as the alginate gel forms. Through numerical simulations and analytical approximations of the downstream behavior, we determine the shape of the fiber in the pipe flow and its impact on the flow velocity as well as on the total production of gel.* [DOI: 10.1115/1.4040833]

## 1 Introduction

The formation of solid like polymeric gel in a flowing liquid is an interesting physical phenomenon. A chemical reaction taking place at the interface between the two flowing liquids produces a solid like gel. The application of such polymeric gel has large scope in biomedics, oil and gas extraction, water treatment, sensors, and other chemomechanical systems. However, continuous production of the gel formation is different to melt-spinning [1,2] because of the emerging interface, but has peripheral analogies with chemical gardens where solid is formed from liquids [3]. In forming these gel fibers, two key questions are: what influences the radius of the fibers and the amount of gel formed?

A widely used cross-linked polymer gel is sodium alginate which is derived from naturally occurring brown seaweeds. One of the special properties of sodium alginate polymer is that when it comes in contact with a divalent cationic solution, the divalent metal ion replaces the sodium ions and acts as a bridge in cross linking several alginate polymer chains together. Typically, calcium chloride solution is used as the binding agent. The chemistry of the cross-linking is described by an irreversible and nearly instantaneous chemical reaction

$$2N_c\mathrm{alg} + N_c\mathrm{Ca}^{2+} \xrightarrow{k_r^*} [\mathrm{alg}\cdot\mathrm{Ca}^{2+}\cdot\mathrm{alg}]_{N_c}$$

Here, alg is the single chain alginate polymer, $N_c$ represents the degree of cross-linking (the egg-box coefficient), and $k_r^*$ is the forward reaction rate constant. So, when the polymer comes in contact with the calcium solution, the positively charged calcium ions diffuse into the polymer solution and bind to the negatively charged polymer, causing the near-instantaneous formation of calcium alginate gel. This gel is solid and can support tensile stresses. The reaction takes place as the two flowing fluids meet with the alginate at the nozzle and the calcium solution in the annular space, forming typically hollow fibers. Mikkelsen and Elgsaeter [4] looked at the one-dimensional (1D) transient solution in planar, axisymmetric, and spherical geometries. They primarily characterized the behavior as a function of reaction rates and initial concentrations. Braschler et al. [5] used the Mikkelsen and Elgsaeter model with experiments to investigate the reaction-front structure by looking for traveling-wave solutions. Models for the gel macroscale structure are described by Kohler and coworkers [6–8]. More recent experimental studies including Secchi et al. [9] and Wu et al. [10] reach different conclusions about reaction front propagating in time, either linearly or classically diffusive, i.e., $\approx t^{1/2}$; but neither of these works combine experiments and modeling as described by Braschler et al. [5].

There have been several reports on the hydrodynamic interaction of two liquids, such as two immiscible fluids at a nozzle [11] or instabilities of immiscible viscously stratified flows [12]. However, the reaction of two fluids forming an emerging solid, a third material, is a challenging problem because the stresses in the new phase need to be spatially resolved in a region of initially zero dimension. In continuous flowing systems, Shin et al. [13] observed that during cross-linked alginate formation, increasing the annular flow reduces the radius of the gel-fiber. A first model with experiments is described by Bonhomme et al. [14], who solve a model for the chemical reaction with a prescribed velocity field. They present a detailed experimental study to characterize the fiber formation conditions and used their model to estimate the density of the gel (cross-linked density of the fiber). In this model, they have focused on the relative velocities of flowing salt and alginate solution as key parameters to control the fiber formation morphology. Using an X-junction with alginate injected into the core and salt solution in two feeder inlets, they investigate the continuous production of fiber. More recent simulations used the reverse configuration of alginate annular flows with the cross linker ($CaCl_2$) in the core [15,16]. However, in both of these works, the chemistry was not coupled to the hydrodynamics and they did not solve for the flow around the nozzle.

Core-annular flows away from the nozzles are well studied, but with minimal attention to flow near nozzles with liquids having

[1]Corresponding author.

Contributed by the Fluids Engineering Division of ASME for publication in the Journal of Fluids Engineering. Manuscript received September 5, 2017; final manuscript received July 10, 2018; published online August 16, 2018. Assoc. Editor: Oleg Schilling.

  

high viscosity contrast [12]. A recent study of core-annular fluid flow used a finite volume scheme to study the case of large viscosity contrast has been investigated [11] and examines the development of the downstream core flow radius as a function of the viscosity ratio, entry flow mean velocity, and Bond and capillary number. Key observations from the model are the Newtonian core fluid expansion near the nozzle and the plug flow at the core. Although the model used in Ref. [11] does not capture the species transport and interface formation, it appears to provide a close analog to the problem we wish to solve. From a different perspective, there is an analogy with the work on chemical gardens [3], where a dissolving metal-salt seed releases metal ions that precipitate with anions in a solution to form a gelatinous colloidal membrane. However, that work is predominantly related to experiments with little attention to modeling. On the other hand, Ref. [1] is a visco-elastic skin model of fiber spinning which does not address the formation of the skin nor the flow near a nozzle. It appears that the generic problem of solid fibers forming from a liquid has not been explored extensively in the past but is important where we need to understand what controls the formation of the emerging interface.

Summarizing, we can say that first, previous works couple (one-way) the fluid mechanics to the chemistry, but do not include feedback from the chemistry to the fluid mechanics; second, solutions are always presented on fixed spatial domains; third, there appears to be very little work on how best to model emerging interfaces. Therefore, from the perspective of an engineering application, the key questions are what controls the mass of gel and its radius. Hence, we find two specific scientific questions to address: (i) How and when does the chemistry interact with the hydrodynamics? and (ii) What is the role of stress in the cross-linked gel?

The aim of this paper is twofold: first, to contrast an immiscible surface-tension (two-phase) model with a miscible chemistry-driven viscous (single-phase) model of this coupled coaxial nozzle emerging interface flow. Second, to investigate what controls the diameter, velocity, and mass of the gel fiber near the nozzle. We therefore use two different models, first the immiscible model, where the gel is represented by a fluid interface with surface tension, and second, as a substitute for gel tension the miscible model, where the viscosity is a function of species concentration so that the chemistry affects the hydrodynamics. This will serve as a basis of a future model which could incorporate both the mechanisms. For both the immiscible and miscible models, we separately present steady-state numerical solutions across a range of parameters that are broadly representative of the studies in Bonhomme et al. [14]. We then compare these simulation results with the solution for the analytical fully developed steady flow condition.

## 2 Model

The present problem is addressed by three different approaches. First, considering a two-phase immiscible model with a sharp fluid–fluid interface (the gel), which includes the impact of the interfacial tension (representing the gel) in the momentum exchange equations. Second, using a single-phase miscible model, which considers a chemical reaction at the contact of the two fluids (alginate and salt solution). Here, the viscosity of the fluid is a continuous function of the diffusing species concentration through the three regimes (alginate, gel, and the salt solution) having advection, diffusion, and reaction. Finally, we present the steady-state fully developed (far-field) flow conditions for the core-annular flow and the scaling relationship describing the gel thickness as a function of the operating conditions.

The fluid mechanics model is common to all three approaches, presented in Sec. 2.1. For the immiscible model, the interface stress conditions and the fluid continuity are described in Sec. 2.2. In the miscible model, we couple the hydrodynamics (two-way) with the advection, diffusion, and reaction, described in Sec. 2.3.

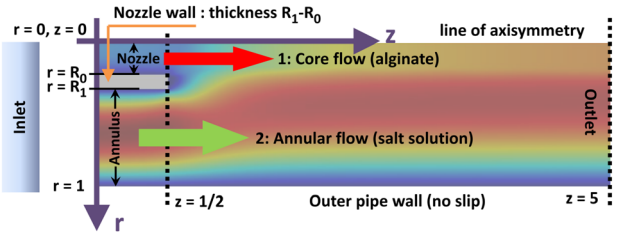


**Fig. 1 Schematic of the geometry of the coaxial domain using nondimensional variables with contours of axial velocity (from Fig. 3): The alginate solution enters through the nozzle (top arrow) and calcium chloride solution (bottom arrow) enters through the annular pipe, where $r = 0$ is the line of symmetry.**

The steady-state fully developed analytical solutions are presented as a special case to the miscible model.

Let us define an axisymmetric coordinate system $r^*$, $z^*$ with time $t^*$, as shown in Fig. 1. The velocity field is $\mathbf{u}^* = u^*(r^*, z^*, t^*)\underline{e}_r + w^*(r^*, z^*, t^*)\underline{e}_z$, with $u^*$ being the outward radial velocity and $w^*$ is the axial velocity component.

We adopt the notation that all dimensional variables have an asterisk superscript. The subscript 1 denotes the property of the fluid injected through the nozzle (core), and the subscript 2 denotes the property of the fluid in the annulus. The flow rate of fluid in the nozzle is defined as $Q_1^* = A_1^* v_b^* \varepsilon$, and likewise, the annular inflow rate $Q_2^* = A_2^* v_b^*$, where $v_b^*$ is the mean annular inflow velocity and

$$\varepsilon = \frac{(Q_1^*/A_1^*)}{(Q_2^*/A_2^*)} \tag{1}$$

is the ratio of the mean nozzle and annular inflow velocities, with nozzle inflow area $A_1^* = \pi(R_0^*)^2$, annulus inflow area $A_2^* = \pi((R^*)^2 - (R_1^*)^2)$, nozzle inner wall at $r^* = R_0^*$, and nozzle outer wall at $r^* = R_1^*$; and outer pipe wall at $r^* = R^*$. Hereinafter, we define $\varepsilon > 1$ as the fast core regime, and $\varepsilon < 1$ as the slow core regime. Key dimensional variables are $R^* = 0.233$ mm; fluid density $\rho^* = 1000\ \mathrm{kgm}^{-3}$; viscosity of salt solution $\mu_2^* = 0.001\ \mathrm{kgm}^{-1}\mathrm{s}^{-1}$; and mean inflow velocity $v_b^* = 0.0125\ \mathrm{ms}^{-1}$. From these variables, we can define axial velocity scale $w_s^* = Q_2^*/(R^*)^2 = A_2^* v_b^*/(R^*)^2 \approx 3.5 \times 10^{-2}\ \mathrm{ms}^{-1}$ (Note: two velocity variables); time-scale $R^*/w_s^* \approx 6 \times 10^{-3}$ s; viscosity scale $\mu_2^*$; surface tension scale $\sigma_{12}^*$; flow rate scale $Q_2^*$; shear-rate scale $w_s^*/R^*$; and body-force scale $\mu_2^* w_s^*/R^{*2}$. Balancing the axial pressure gradient to the lateral viscous stresses, we have pressure scale $w_s^* \mu_2^*/R^*$.

For each parameter combination, the transient fluid model is time-stepped from a given initial condition to the steady-state solution. Hereinafter, all equations are given in nondimensional variables, which are denoted without an asterisk superscript, unless otherwise stated. This description reflects our use of two different commercial modeling packages. For the miscible model, we prefer the finite-element based COMSOL® v5 for its adaptability in handling multiphysics problems. For the immiscible model, we select the finite volume based FLUENT v16 for its efficiency in handling fluid–fluid interface problems.

**2.1 Fluid Motion.** The fluid flow field is modeled with the incompressible Navier–Stokes equations

$$Re\left(\frac{\partial \mathbf{u}}{\partial t} + \mathbf{u} \cdot \nabla \mathbf{u}\right) = \nabla \cdot \mathbf{T} + \mathbf{F}, \qquad \nabla \cdot \mathbf{u} = 0 \tag{2}$$

where Re is the Reynolds number defined by $\mathrm{Re} = \rho^* Q_2^*/(R^* \mu_2^*)$; $p = p(r, z, t)$ is the pressure; $\mathbf{T}$ is the total stress tensor in the fluid given by

$$\mathbf{T} = -p\mathbf{I} + \mu\dot{\boldsymbol{\gamma}} \tag{3}$$

$$\dot{\boldsymbol{\gamma}} = \nabla\mathbf{u} + (\nabla\mathbf{u})^{\mathrm{T}} \tag{4}$$

such that T denotes the transpose, $\mathbf{I}$ is the identity matrix, $\dot{\boldsymbol{\gamma}}$ is the rate of strain tensor, and $\mu$ is the viscosity of the fluid. From this, the magnitude of the shear rate is defined by

$$\dot{\gamma} = \sqrt{\frac{1}{2}(\dot{\boldsymbol{\gamma}} : \dot{\boldsymbol{\gamma}})} \tag{5}$$

Based on this, we can define the Carreau–Yasuda law

$$\mu = 1 + (\mu_p - 1)[1 + (\lambda\dot{\gamma})^2]^{(m-1)/2} \tag{6}$$

where $\dot{\gamma}$ is the shear rate, $\lambda$ is the shear-rate parameter, and the shear-rate dependence is described by the Carreau–Yasuda law. As an example, and for clarification purposes, we note here that $\mu$, $\mu_p$, $\lambda$, and $\dot{\gamma}$ are nondimensional variables; these are connected to their dimensional counter parts via $\mu = \mu^*/\mu_2^*$; $\mu_p = \mu_p^*/\mu_2^*$; $\lambda = \lambda^* w_s^*/R^*$; $\dot{\gamma} = \gamma^* R^*/w_s^*$; such that $\lambda^*$ has units of s and $\gamma^*$ has units $\mathrm{s}^{-1}$. The dimensionless parameter $m > 1$ specifies the fluid is shear thinning. The zero shear viscosity ($\mu_p$) is a function of the species concentration as described in the miscible model (Sec. 2.3, Eq. (15)), but is constant for the case of immiscible model (Sec. 2.2).

At the nozzle inlet, we have a prescribed laminar inflow rate $Q_1 > 0$, and at inlet 2, we have the flow rate $Q_2 = 1$ as a result of the nondimensionalization. Thus

$$Q_1 = 2\pi\int_0^{R_0} wr\,\mathrm{d}r, \quad Q_2 = 2\pi\int_{R_1}^{R} wr\,\mathrm{d}r = 1 \tag{7}$$

At the outlet, for the flow, we specify the normal component of the stress

$$\mathbf{T}\cdot\mathbf{n} = -p_0\mathbf{n}, \quad p_0 \le 0 \tag{8}$$

where $\mathbf{n}$ is the normal vector pointing outward from the domain. We do not impose a constraint on the tangential component of the stress. On the geometric walls for the fluid, we impose no-slip and no-penetration boundary conditions

$$\mathbf{u} = (u, w) = 0 \tag{9}$$

The initial condition is given by

$$u(r, z, 0) = w(r, z, 0) = 0 \tag{10}$$

**2.2 Immiscible Model.** The present situation is a classical case of modeling the interface between two immiscible fluids [17]. The jump in the stress continuum across the interface is balanced by the surface tension forces. The continuity of the velocity field and the stress (both tangential and normal) at the fluid–fluid interface (on contact of the alginate with salt solution) is

$$\mathbf{u}_1 = \mathbf{u}_2 \tag{11}$$

$$\mathbf{n}_1\cdot\mathbf{T}_1 - \mathbf{n}_2\cdot\mathbf{T}_2 = \frac{\mathrm{Re}}{\mathrm{We}}(\nabla_t\cdot\mathbf{n}_1)\mathbf{n}_1 \tag{12}$$

where $\mathrm{We} = \rho w_s^{*2} R^*/\sigma_{12}^*$ is the Weber number. Here, the subscript $i = 1$ and 2 denotes the core (alginate) and annulus (salt solution), respectively. The fluid velocity field for the respective domain is already described in Eq. (2) and viscosity relation is Eq. (6). The zero-shear viscosity ($\mu_p$) is related to the constant alginate concentration $C_2$ (in domain 1) as $\mu_p = 1 + b_d C_2$, and for the salt solution (domain 2), $\mu_p = 1$. The present set of equations is solved in the three-dimensional domain using a continuous surface force method (CSF) as described in Appendix C, together with the volume of fluid (VOF) scheme considering it as a two phase flow. However, this model does not capture the effects of the gel formation and its growth downstream. This is modeled (using a different approach) with the change in viscosity (where the gel is considered to effectively have infinite viscosity) as a function of the diffusing species across the interface, described in detail in Sec. 2.3.

**2.3 Miscible Model.** In the miscible model, we solve the advection-diffusion-reaction equation for the concentration of the three species $C_i^* = C_i^*(r^*, z^*, t^*)$: Alginate concentration $C_1^*$; Salt concentration $C_2^*$; and cross-linked alginate gel concentration $C_3^*$. Here, we assume that the three species have constant diffusivities $D_i^* = (D_2^*/10, D_2^*, 0)$; these diffusivities are discussed in further detail at the start of Sec. 4, excepting the gel which is solid and assumed to be nondiffusive. We also assume that a reaction source term $S_i^* = S_i^*(C_i^*)$ is the rate of production (positive) or consumption (negative) of each species, where the rate of reaction is $\kappa_r^*$, as defined in Sec. 1. Here, we choose the reaction chemistry to follow the model identified by Mikkelsen and Elgsaeter [4], except we have constant diffusion. Here, we scale the species concentrations with the initial salt concentration $C_{20}^*$; diffusivity with the salt diffusivity, $D_2^*$; and the reaction source term with $\kappa_r^* {C_{20}^*}^3$. We then represent the time-dependent advection-diffusion-reaction equation in the corresponding nondimensional variables for the evolution of the species as

$$\frac{\partial C_i}{\partial t} + \mathbf{u}\cdot\nabla C_i = \frac{D_i}{\mathrm{Pe}}\nabla^2 C_i + \beta_r S_i \tag{13}$$

where Peclet number $\mathrm{Pe} = w_s^* R^*/D_2^*$, nondimensional diffusivity $D_i = (0.1, 1, 0)$, and reaction scale $\beta_r = \kappa_r^* R^* {C_{20}^*}^2/w_s^*$ are the nondimensional parameters. The three components of the reaction rate vector $S_i$ are

$$S_i = (-\eta, -N_c\eta, \eta) \quad \eta = C_2 C_1 (C_1 + C_3) \tag{14}$$

where $N_c \sim O(1)$ is the dimensionless stoichiometric coefficient, as described in Sec. 1. The function $\eta$ is greater than zero only when both the salt $C_2 > 0$ and the alginate $C_1 > 0$. One can note that the reaction is second order in alginate concentration and first order in gel concentration $C_3$.

Next, the fluid viscosity ($\mu$) is coupled to the species concentration via the zero shear viscosity ($\mu_p$) in Eq. (6)

$$\mu_p = 1 + b_d(C_1 + \alpha C_3) \quad 0 \le C_1 \text{ and } 0 \le C_3 \tag{15}$$

where $b_d = b_d^* C_{20}^*/\mu_2^*$, and constant $b_d^* \approx 3.077\,\mathrm{Pa}\cdot\mathrm{s/M}$ indicates the rate of change of viscosity with alginate concentration. The dimensionless parameter $\alpha$ governs the impact of the cross-linking on gel-fiber viscosity. The dependence of $\mu_p$ on gel concentration (in Eq. (15)) is the simplest model to hypothesize how cross-linking increases viscosity. This is a first step toward understanding how the flow field is affected by the reaction (a future model might include visco-elastic responses).

The partial differential equation in Eq. (13) is solved subjected to the following boundary conditions. At inlet 1, the concentration of alginate is fixed as $C_{10}$, and the concentration of salt $C_{20}$ is fixed at inlet 2

$$C_2(R_1 \le r \le R, 0, t) = C_{20} \quad C_1(0 \le r \le R_0, 0, t) = C_{10} \tag{16}$$

At the outlet, we impose a Neumann boundary condition

$$\mathbf{n}\cdot D_i\nabla C_i = 0 \tag{17}$$

while at the no-slip wall boundary, the effective zero species flux condition is satisfied

$$\mathbf{n} \cdot (\mathbf{u}C_i - D_i \nabla C_i) = 0 \tag{18}$$

The following initial conditions are used to solve Eq. (13):

$$C_2(R_m \le r \le 1, z, 0) = C_{20} \quad C_1(0 \le r \le R_m, z, 0) = C_{10}$$
$$C_3(r, z, 0) = 0 \tag{19}$$

where $R_m = (R_0 + R_1)/2$, with constants $C_{10}$ and $C_{20}$ specified later. Note that several different types of initial conditions were explored; however, to expedite attaining a steady-state numerical solution, the above conditions are found to be best.

*2.3.1 One-Dimensional Steady-State Far-Field Co-Annular Analytical Models.* In this section, we present a simplified model from the force balance on the fiber and the far-field (far downstream of the nozzle) velocity profiles where $u \to 0$ and $z \to \infty$. At the fiber interface $r = R_g$, the two flow regions are divided, such that in $0 \le r \le R_g$ we have only the gel moving with velocity $w_1 = w_1(r)$ and $C_1 = 0$, $C_2 > 0$, $C_3 > 0$, $\lambda = 0$, so $\mu = \mu_1 = 1 + b_d \alpha C_3$.

While for the region $R_g < r < 1$, with $w = w_2(r)$, we have only salt solution $C_1 = 0$, $C_2 > 0$, $C_3 = 0$, $\lambda = 0$, having $\mu = \mu_2 = 1$. We solve the 1D steady-state Stokes equation (dropping the inertial terms in Eq. (2) as they reduce to zero in the far-field fully developed limit) using the following boundary conditions:

(i) symmetry at $r = 0$, $\mathrm{d}w_1/\mathrm{d}r = 0$;
(ii) no-slip on $r = 1$, $w_2 = 0$;
(iii) velocity continuity on $r = R_g$, $w_1 = w_2$ and
(iv) continuity of the shear-stress (without any surface tension in Eq. (12)).

This combination of the boundary conditions balances the tangential and normal stress on the core flow, hence it represents a *no net-force* equilibrium solution. Maintaining the same pressure gradient across both flows and matching shear stress at $r = R_g$, we recover

$$\frac{\mathrm{d}p}{\mathrm{d}z} = -\frac{8}{\pi\left(R_g^2 - 1\right)^2} \tag{20}$$

The prediction for the pressure gradient differs from the prediction of Bonhomme et al. [14] (Eq. (11) therein) by a factor of $(1 - R_g^2)^{-1}$. This factor, absent in Bonhomme's prediction, is required for the integral of the fluid flux over the annulus to be equal to the mass flow rate. The fiber radius $R_g$ is given by the (smaller root) solution of

$$\left(1 - \frac{1}{2\mu_1} + \frac{Q_1}{2}\right)R_g^4 - (1 + Q_1)R_g^2 + \frac{Q_1}{2} = 0 \tag{21}$$

In the limit $\mu_1 \to \infty$, we can compute the alginate plug-velocity and fiber radius to be

$$w_1(r = R_g) = \frac{2 + Q_1}{\pi} \quad R_g = \left(\frac{Q_1}{2 + Q_1}\right)^{1/2} \tag{22}$$

*2.3.2 Gel Mass Scaling Law in a Fully Developed Flow Field.* Let us define the cross-sectional mass integral $M_i(z, t)$ for each of the species as

$$M_i(z, t) = 2\pi \int_0^1 r C_i(r, z, t)\, \mathrm{d}r \tag{23}$$

An estimate for the rate at which the mass of gel ($M_3$) changes downstream can be obtained in the region where the flow is fully developed with an ongoing reaction. Note gel mass $M_3(z, t)$ is related to the link density defined by Bonhomme (Eq. (19) therein). The complexity of the problem is significantly reduced with the assumptions that the cross-linking reaction time-scale is much faster than the salt diffusion timescale and the diffusivity of the alginate is much less than that of the salt. With these assumptions, the rate of change of the gel mass in the axial direction is approximately

$$\frac{\partial M_3}{\partial z} \approx \frac{R_g}{N_c w_1 \mathrm{Pe}} \frac{\partial C_2(R_g, z)}{\partial r} \tag{24}$$

where $M_3$ is the mass of gel, Pe is the Peclet number of the salt, $w_1$ is the fully developed alginate velocity (Eq. (22)), and $R_g$ is the radius of the gel sleeve (Eq. (21)). The full derivation of Eq. (24) and the equations to follow can be found in Appendix B. Moreover, we can approximate the flux $\partial C_2/\partial r \approx (C_{20} - 0)/2\delta$, where $\delta$ corresponds to the length-scale of the salt depleted region surrounding the alginate/gel core. Due to the large Péclet numbers associated with typical gel fiber experiments, this depleted region will be within some boundary layer with length inversely related to the Péclet number. With this species flux approximation, $\partial M_3/\partial z$ in Eq. (24) is simplified to

$$\frac{\partial M_3}{\partial z} \approx \frac{R_g C_{20}}{2 N_c w_1 \delta \mathrm{Pe}} \tag{25}$$

We expect $\delta$ to be approximately constant as long as Pe does not change by much; the specific value of $\delta$ used is detailed later in the discussion of Fig. 2(*d*).

## 3 Computational Details

**3.1 Immiscible Two Phase Surface Tension Model.** The system of equations is solved using a commercial fluid dynamics solver—FLUENT v16, based on finite volume discretization, following the CSF method as described in Appendix C, together with the VOF scheme representing it as a two phase flow. It may be mentioned here that the solution domain in this case is the full three-dimensional geometry. The momentum equation is discretized using the quadratic upstream interpolation for convective kinematics (popularly known as QUICK) scheme [18], a higher-order differencing scheme based on the weighted average of second-order-upwind and central interpolations of the variable. First-order explicit transient solver is used to solve the system, together with the Geo-Reconstruct scheme [19] for interpolation of the phase variables at the interface, to avoid numerical interfacial diffusion. The geometric reconstruction scheme represents the interface between fluids using a piecewise-linear approach and uses

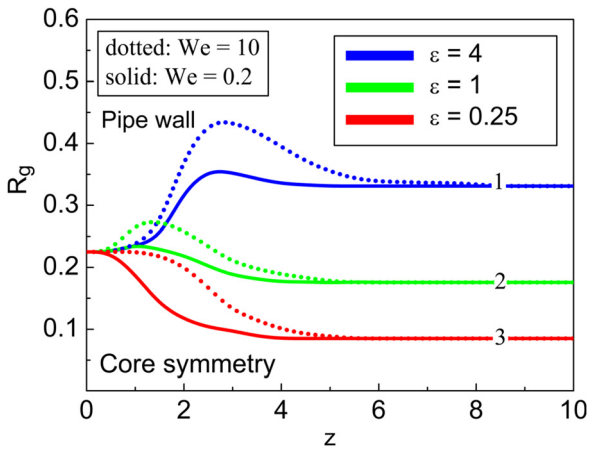


**Fig. 2 Profile of the fiber radius along the axial length of the device with the velocity ratio (with respect to the core and annular flows) as a parameter**

this linear shape for calculation of the advection of fluid through the cell faces. This scheme is the most accurate, robust, and is applicable for general unstructured meshes. Since the flow in the present case is dominated by body forces rather than pressure gradients, a body-forced weighted scheme with "pressure implicit with splitting of operators" (PISO) algorithm is used for pressure correction [20], which is an extension of the SIMPLE algorithm [21] used for solution of the Navier–Stokes equation. The PISO algorithm shifts the repeated calculations required by SIMPLE and SIMPLEC inside the solution stage of the pressure-correction equation [20]. After one or more additional PISO loops, the corrected velocities satisfy the continuity and momentum equations more closely. The algorithm is slightly more CPU intensive, but dramatically reduces the number of iterations required for convergence, especially in transient problems. Simulations were initiated with very small time steps and these were increased gradually for later times with no resultant spurious numerical oscillations in the solution. The solution was assumed to have reached a steady-state when the root-mean-square error between the interface profiles for successive time steps was found to be $<10^{-4}$.

The computational domain was meshed using unstructured hexagonal mesh elements with more refinement along the inner–outer fluid contact boundary. Grid independence was tested at various mesh sizes starting from 0.00013 to 0.0095, as evidenced in Fig. 3. It was observed that the interface and fully developed core radius were unchanged for dimensionless mesh sizes less than 0.0021. Hence, the mesh size of 0.0021 was considered adequate for the current numerical simulations. The core liquid region including the interface has a dimensionless minimum and maximum mesh size of 0.00045–0.0021, with an average skewness of $0.78 \pm 0.13$. Similarly, the remaining geometry has minimum to maximum mesh size range of 0.0013–0.0061, with the average skewness of $0.73 \pm 0.19$. The simulations were run on a Linux IBM machine with 36 cores ($2 \times 18$ Core Intel with hyperthreading) (using only eight cores), with a clock speed of 2.3 GHz utilizing up to 24 GB of the available 768 GB of RAM. Total computational time is effectively around 1.1 h.

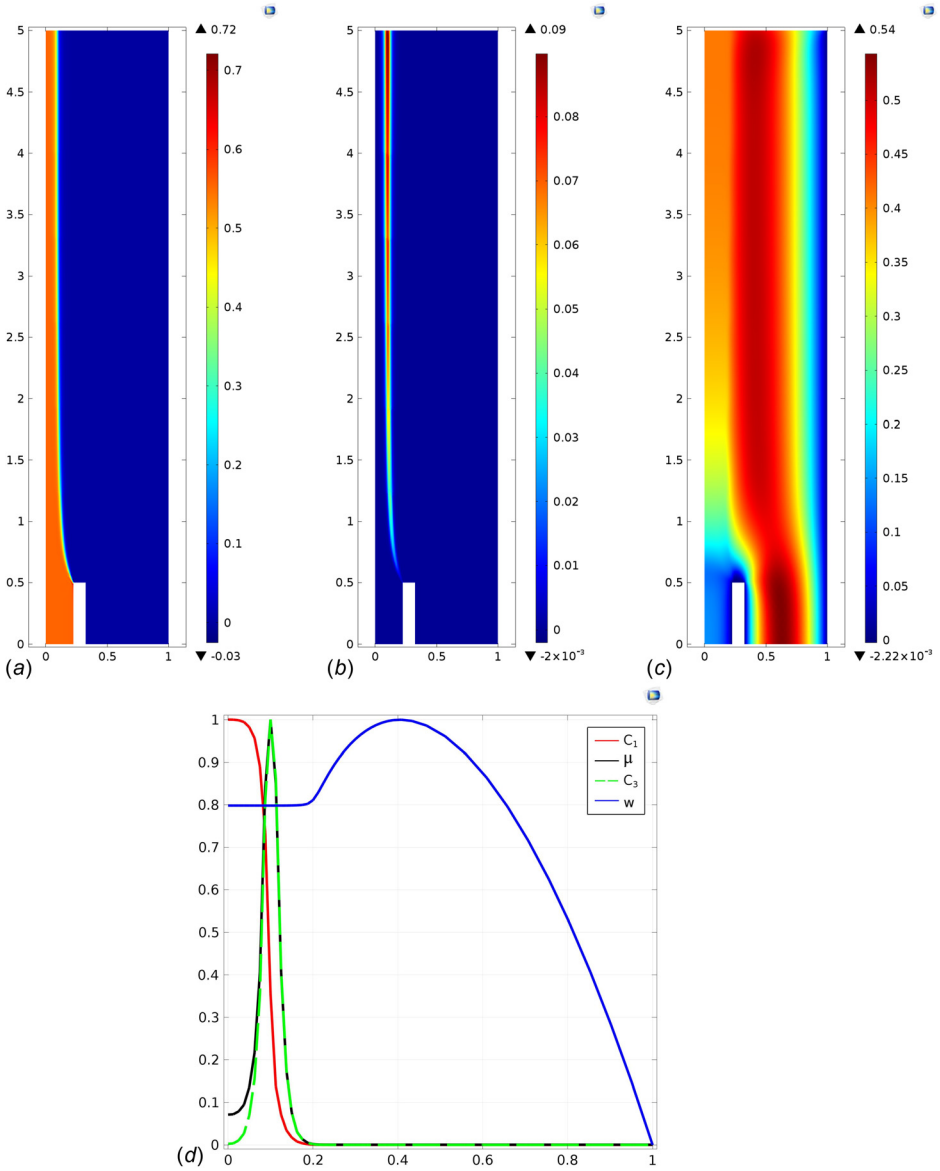


**Fig. 3 At steady-state, for $\alpha = 100$ and $\varepsilon = 0.25$, the contour profiles of (*a*) alginate concentration—$C_1$, (*b*) gel concentration—$C_3$, and (*c*) axial velocity—*w*. Separate shading scales for each image. In (*d*), we show a radial slice through these and other properties at $z = 4$; note, each data set is scaled differently, corresponding to its maximum value to make their variation apparent on the same axis scale.**

**3.2 Single Phase Miscible Species Transport Model.** The governing equations for this model have been solved in the two-dimensional axisymmetric system using the commercial finite element method package COMSOL v5. Two modules have been used in solving the governing equations: The "Laminar Flow Module" and the "Transport of Dilute Species Module." Below, we discuss some key features of the modules and solver settings that have been used to solve the miscible model.

The Navier–Stokes equations were solved using a projection method. A second-order backward difference formula was used for all temporal integration. The linear basis functions were used to discretize both the velocity and pressure variables in the Navier–Stokes equations. Linear basis functions were also used to discretize the species transport equations. The viscosity model used was the inbuilt Carreau model, with the zero shear-rate viscosity parameter computed based on the species concentration. The time-stepping used streamline and cross-wind diffusion to stabilize the solution. The default tolerances were used with absolute precision of $5 \times 10^{-4}$ and relative precision of $10^{-2}$. The full set of equations was solved using a fully coupled method, which used the PARDISO solver, with the Jacobian updated every time-step, and termination based on tolerance. Two additional helper ordinary differential equations (ODEs) were used in the implementation of the inflow boundary conditions. The solutions were all computed on a free triangular mesh. We used a relatively coarse mesh of two sizes: in the gelled region, we used a maximum element size of 0.0125, and away from the gelled region, we used a maximum element size of 0.05. These choices imply we under-resolve the Peclet number boundary layer, but they adequately capture the qualitative nature of the flow. The mesh refinement study presented in Appendix A demonstrates this point. The simulations for the six parameter combinations presented in Fig. 4 were run using 4 of 8 cores on a 3 GHz Core i7-493 DELL Precision M4800 running Windows 7 utilizing up to 2 GB of the available 32 GB of RAM in a total of 4 h; each simulation with $\alpha = 100$ typically takes about twice the time of an $\alpha = 1$ simulation.

## 4 Results and Discussion

Here, we present the result for the three models. First, we describe in detail the behavior observed in the immiscible fluid model; second, we describe the observations in the immiscible model; third, we compare the two models with results from the far-field analytical model. Here, we choose to look at the behavior of the system in a parameter regime similar to that used by Bonhomme et al. [14,22]. We now comment on the main constants in the models:

(i) Salt diffusivity $D_2^*$ and properties. For $Ca^{2+}$ ions in water values of $D_2^*$ used by previous authors range between $2.5 \times 10^{-9}$ $m^2$ $s^{-1}$ in Ref. [22] and $8.3 \times 10^{-10}$ $m^2$ $s^{-1}$ in Ref. [5]. As a lower bound, we choose $D_2^* = 10^{-10}\,m^2\,s^{-1}$. For 1% w/v salt solution, we use a mass of 110.98 g/M $CaCl_2$ which at concentration $C_{20}^* = 1\%w/v$ gives $C_{20} = 0.09M$.

(ii) Alginate diffusivity $D_1^*$ and properties. Values quoted by the previous authors range from $D_1^* = 1 \times 10^{-12}\,m^2\,s^{-1}$ in Ref. [4] to $D_1^* = 2.5 \times 10^{-12}\,m^2\,s^{-1}$ in Ref. [14]. From these works and others, $D_1^*$ is commonly discussed to be an order of magnitude smaller than the salt diffusivity, this motivates our statement at the start of Sec. 2.3, to assume $D_1^* = D_2^*/10$. We also choose for 1% w/v 200 g/M alginate a zero-shear rate viscosity of $\mu_p^* = 153$ cp, $m = 0.4$, and $\lambda^* = 0.1$ s, which gives $C_{10} = 0.555$ and $b_d \approx 277$.

(iii) Reaction rate $\kappa_r^*$. The work by Mikkelsen and Elgsaeter [4] notes the value to be very uncertain but they choose $\kappa_r^* = 0.02\,M^{-2}s^{-1}$. We follow the more recent work of Braschler et al. [5] and choose $\kappa_r^* = 5300\,M^{-2}s^{-1}$.

(iv) Stoichiometric coefficient $N_c$. Previous authors [5,14], respectively, offer values of $N_c = 3.42$ and $N_c = 3.33$; we choose $N_c = 3.4$.

Based on the above choices for our system, we have Reynolds number Re $\approx 8.1$, Peclet number Pe $\approx 8.1 \times 10^4$, and reaction scale $\beta_r \approx 0.28$.

Looking at Eq. (1), we recall that since the annulus flow rate $Q_2^*$ is held fixed, the core flow rate $Q_1^*$ increases with $\varepsilon$ and vice versa. In both the immiscible and miscible model results presented here, we vary the core flow rates for $\varepsilon = 4$, 1, and 0.25.

**4.1 Immiscible Model Results.** The effect of surface tension on the interface curvature without any interfacial chemical reaction or mass transfer is illustrated in Fig. 5. The effect of the

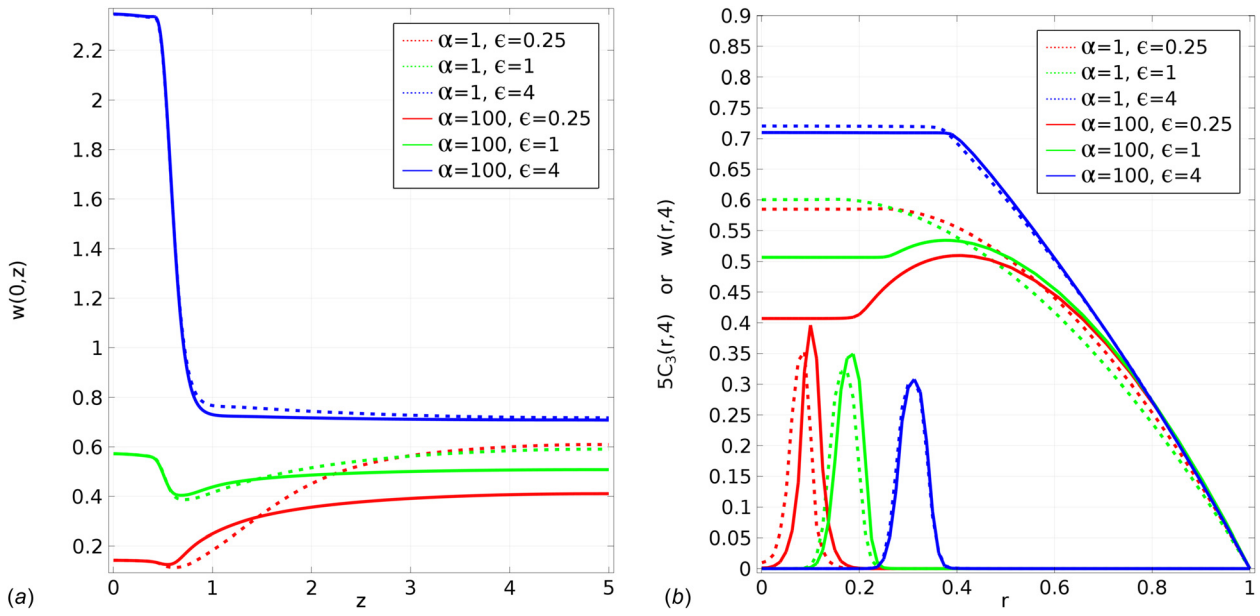


**Fig. 4 Here, we show the impact of varying $\alpha = 1$ and 100 and $\varepsilon = 0.25$, 1 and 4 on the axial velocity along (*a*) *w*(0, *z*) and (*b*) *w*(*r*, *z* = 4); figure (*b*) also shows the corresponding gel concentrations $C_3$ on the same axis multiplied by five for easy viewing. Across both figures, solid lines are solutions for $\alpha = 100$ and dotted lines solutions for $\alpha = 1$. Within these two categories, we use the same line shading for each value of $\varepsilon$.**

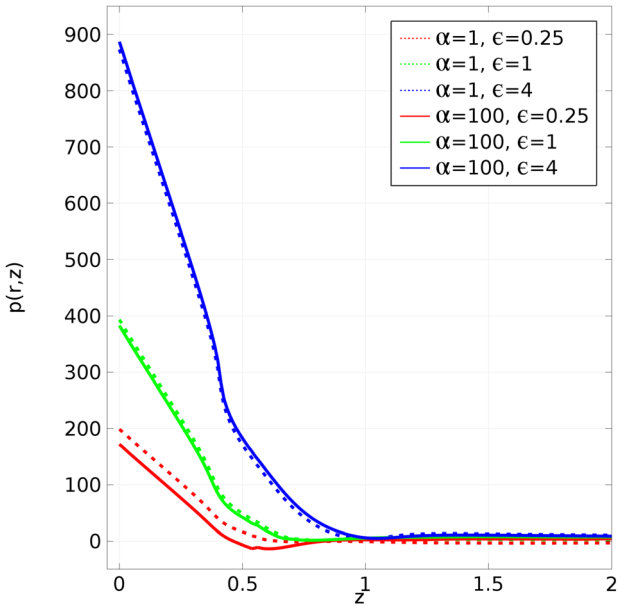


**Fig. 5 The pressure $p(r, z)$ along the centerline $r = 0$ for the wall six combinations of $\alpha$ and $\epsilon$**

surface tension is defined through the magnitude of We, which in this case is 0.2 and 10. The Weber number defines the relative magnitude of the inertia to surface forces. It is evident from Fig. 5 that increasing the surface tension suppresses the impact of the core flow on the interface near the nozzle. As described previously, when $\varepsilon$ increases, the core fluid flux increases; this results in an enlargement of the cross section occupied by the core fluid. We checked that in the case $m = 1$ in Eq. (6), the present result is similar to the result of Vempati et al. [11] (note that in both of these works, the range of parameters chosen are different). The key differences are as follows: (i) the core fluid considered in this case is shear thinning, which possibly explains the reason for the apparent large difference of the expansion of the core fluid (for $\varepsilon > 1$) which is less apparent in the work of Vempati et al. [11]; (ii) the effect of different values of surface tension is shown, whereas the work of Vempati presents the results with only one surface tension; and finally, (iii) the effect of hoop stress (circumferential stress) due to surface tension [23] is not considered in the work by Vempati et al. [11]. The far stream condition satisfies the result of the simplified 1D model, which shows that surface tension has no effect there. Details of the quantitative comparison of the results with the other models are described in Sec. 4.3.

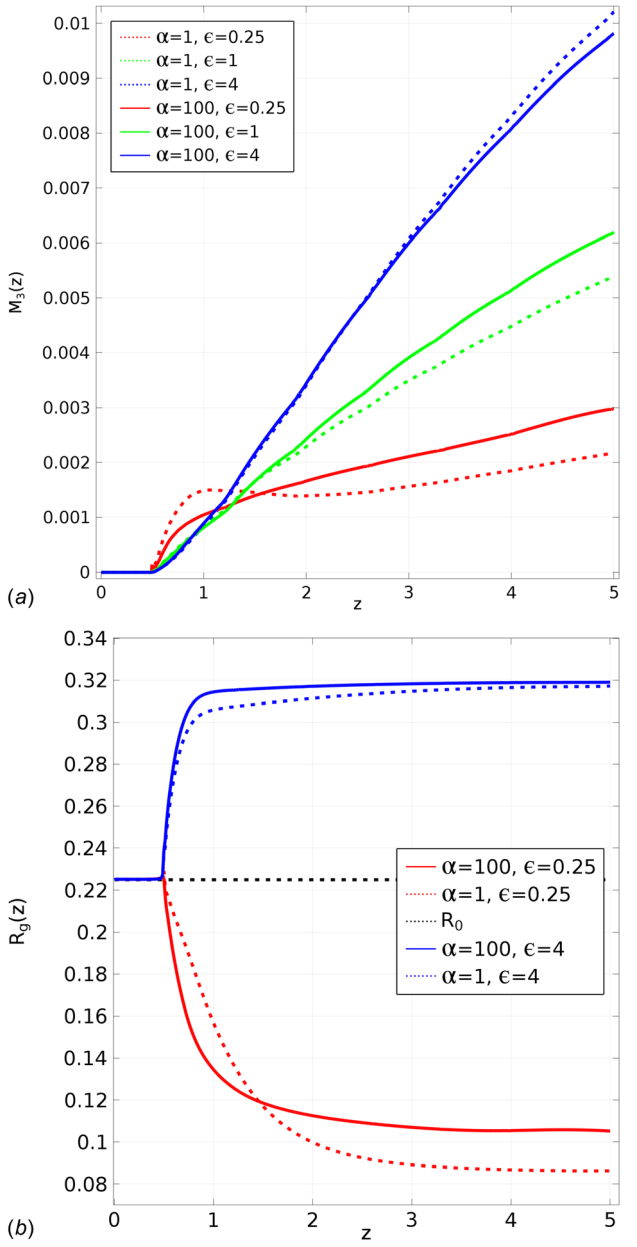


**Fig. 6 In (*a*), the cross section mass of gel $M_3(z)$. In (*b*), the effective fiber radius $R_g(z)$.**

**4.2 Miscible Model Results.** To illustrate the impact of reaction on the flow, we choose two different cases, $\alpha = 1$ and 100; here, the viscosity depends on the alginate and gel concentration, and $\alpha$, as seen in Eq. (15). Unless otherwise noted, we show results at a time $t = 40$, when the system has reached steady-state.

Initially, we will show some specific results for the slow core regime case $\varepsilon = 0.25$ and a strong effect of the alginate concentration on viscosity for $\alpha = 100$. These features are representative of the typical system behavior, except in certain cases which we will identify. In Figs. 6(*a*)–6(*c*), we show the contour profiles of the axial velocity, alginate, and gel concentration. The qualitative features we observe at a fixed $z$ downstream of the nozzle are (i) radially constant alginate concentration in the core region, and radially constant salt concentration in the annular region; (ii) between the core alginate and outer salt solution, we see the creation of a gel region, which becomes thicker in the downstream; (iii) a radially constant plug velocity profile in the core region; and (iv) a rapid contraction of the alginate fiber radius at the nozzle outlet. We attribute (iii) to the high inlet core alginate viscosity. The core region axial velocity changes rapidly from exiting the nozzle and evolves toward the annular flow velocity profile through momentum exchange.

We shall now look at more specific features. In Fig. 6(*a*), in this specific case of $\varepsilon = 0.25$, the velocity of the alginate increases as $z$ increases. We observe correspondingly in Fig. 6(*b*) that as the core flow is accelerated, the region of near-constant alginate concentration decreases in width, this is due to alginate mass conservation. In Fig. 6(*c*), the mean velocity of the annular flow will decrease as the area it occupies increases. We also note that the alginate concentration stays almost constant near $r = 0$. At the nozzle exit, the edge of the alginate forms from the inside corner of the nozzle; this is because the annular velocity is higher than core alginate and transfers momentum to it. In Fig. 6(*b*), we see that the gel begins to form as soon as the alginate and salt solutions meet. Since the simulations under-resolve the Peclet number boundary layer, we only interpret gel concentration as seen in Fig. 6(*b*) qualitatively; grid refinement simulations demonstrate qualitative accuracy (Appendix A).

In Fig. 6(*d*), we show a radial slice far downstream of the nozzle illustrating axial velocity, species concentrations, and the total viscosity, all rescaled by their different maximum values. Consistent with the two-dimensional plots we have shown in Figs. 6(*a*)–6(*c*), we see that we have plug flow velocity where the alginate or gel concentration is much bigger than zero. We also observe that on increasing the gel concentration, the fluid viscosity is correspondingly much bigger, with both variables peaking at the same radial value far downstream of the nozzle. Although not shown here, inspection of the radial component of velocity shows that it is about 1% of the value of the axial component, i.e., the solution is still slowly evolving in the axial direction.

*4.2.1 Impact of Inflow Ratio ε and Reaction α on Velocity Profile.* The characteristics of the axial and radial velocity profiles, gel mass and radius for different parameter regimes are illustrated in Fig. 4.

In Fig. 4(*a*), for $\alpha = 1$ we notice that, away from the nozzle, the centerline velocity $w(0, z)$ always decreases immediately on exiting the nozzle. There are two reasons for this.

First, inside the nozzle, we have a quasi-parabolic velocity profile which is zero on the nozzle wall, however, once outside the nozzle, we rapidly move to a plug velocity profile; hence, the same volume flux gives a lower axial velocity on $r = 0$. This rapid change in velocity profile happens because the axial pressure gradient inside the nozzle is much larger than the axial pressure gradient in the annulus (due to large alginate viscosity compared to the salt solution). This can be seen in Fig. 7 where we show the pressure on the centerline ($r = 1$) for the six combinations of $\varepsilon$ and $\alpha$. As $z \to 0$, the pressure gradient has a large constant value which is representative of the higher viscosity fluid moving in the narrower nozzle. As $z \to 5$, the pressure gradient has a much lower value which represents the axial motion of the alginate-gel lubricated by the much lower annular viscosity salt solution. In between these two regimes, we see a transition where the evolving pressure gradient is consistent with work done in the relative expansion or contraction of the alginate gel. This change in pressures near the nozzle is consistent with the changes in fiber radius as discussed further in Sec. 4.2.2.

Second (and in combination), the influence of the annular flow either accelerating the core when $\varepsilon < 1$ or decelerating the core when $\varepsilon > 1$. While the center velocity-profile equilibrates within a few nozzle diameters, the axial momentum exchange between the fiber and the annular salt continues downstream of the nozzle over a much longer length scale (we address this question more specifically in Sec. 4.4.3, where we compare different models). For small $\varepsilon$ sufficiently downstream of the nozzle, the core flow begins to accelerate resulting in radial contraction of the alginate-gel. Conversely, for larger $\varepsilon$, we have radial expansion and axial deceleration. Further, as we increase $\alpha$ (from 1 to 100), the axial velocity approaches equilibrium faster for small values of $z$. As the reaction proceeds ($\alpha > 1$), it generates a skin of higher viscosity gel, which further resists deformation by the (faster or slower) annular flow.

In Fig. 4(*b*), we show two different quantities: the radial variation of the axial velocity $w(r, 4)$ and the gel concentration $5C_3(r, 4)$ profiles far downstream of the nozzle. Here, the gel

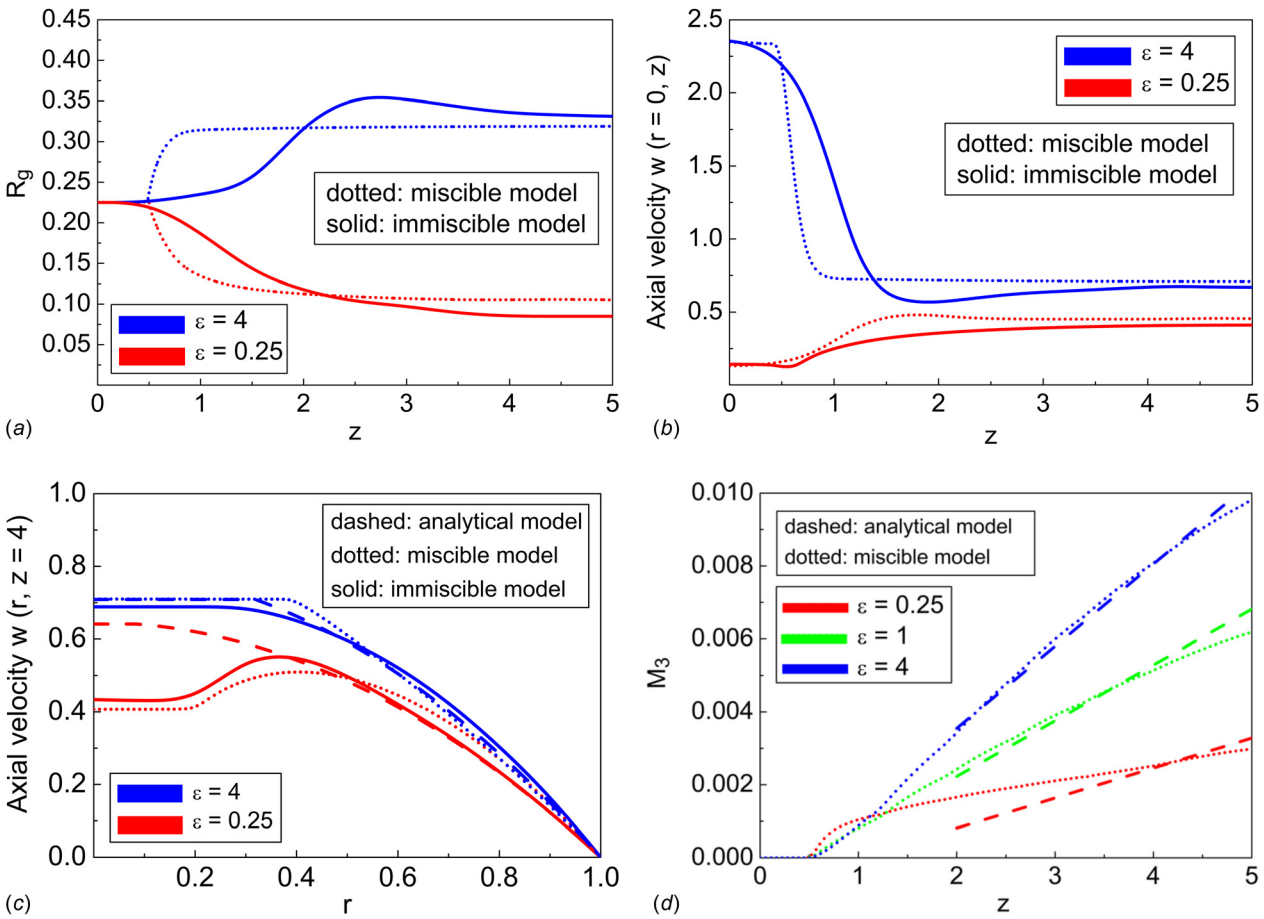


**Fig. 7 Comparison of the (*a*) fiber radius; (*b*) axial velocity profile at the centerline ($r = 0$) using two different model approaches—single phase miscible species reaction model ($\alpha = 100$) and the two-phase immiscible surface tension model corresponding to $We = 0.2$; (*c*) comparison of the radial velocity profile downstream ($z = 4R$) for all the three different models; and (*d*) spatial gradient of the gel mass with $z$ (Eq. (25)) using the simplified 1D analytical steady-state model and the miscible species reaction model. Across these four graphs, the same line shade is used for each data set.**

concentration is multiplied by five so it is visible on the same $y$-axis scale as $w(r, 4)$. We can see here the spatial transition of the core flow to the annular flow, which identifies the edge of the core flow. For given $\varepsilon$, increasing $\alpha$ permits the gel layer to support a greater change in shear stress from the core to the annulus. This reconfirms the perspective we see in Fig. 4(*a*): that increasing the gel viscosity slows down the axial development of the flow. We see that the edge of the gel matches the edge of the core flow region. We demonstrate in Appendix A that under grid refinement, the center of gelled region converges and that the edge of the gel is consistent with the edge of the core flow. The above suggests that on a finite domain, we can have independent flows on either side of the gel, which will more slowly equilibrate and which may ultimately support different pressure gradients. This is consistent with the broader transition of the viscous–viscous fluid toward a viscous-solid fluid regime. In Appendix E, we present scaled species flux data to demonstrate that far away from the nozzle, the flows are dominantly axial.

*4.2.2 Impact of Inflow Ratio $\varepsilon$ and Reaction $\alpha$ on Mass and Radius.* Here, we can begin to look at the impact of the chemistry on the flow. In Fig. 8(*a*), for small $\varepsilon$, we see that the total mass of gel $M_3(z)$ close to the nozzle reduces on increasing $\alpha$; this is because increasing $\alpha$ leads to fiber acceleration and a reduction in its radius. Hence, there is a smaller alginate surface area, and consequently, less influx of salt and so less gel. However, once sufficiently downstream from the nozzle, we also observe that increasing $\alpha$ slows down the core flow, and hence, increases the total mass of alginate and gel as seen in the cases $\varepsilon = 0.25$, 1. Whereas for $\varepsilon = 4$, increasing $\alpha$ reduces the mass of gel, as the increased gel viscosity inhibits the expansion of the alginate associated with the axial flow compression. The conclusion is that in extensional flows (i.e., slow core, $\varepsilon < 1$), the mass of gel increases with $\alpha$ by slowing the core flow and increasing the cross-sectional area of alginate and gel. Conversely in flows such as $\varepsilon = 4$, increasing $\alpha$ reduces gel production. The caveat to these results is that the process may not be monotonic because of flow adjustment at the nozzle. Therefore, in order to maximize the mass of gel (which might also strengthen the fiber mechanically), we need to minimize $\alpha$ and maximize $\varepsilon$.

Since the concentration of alginate is nearly radially constant at a fixed $z$ (as the mass transfer boundary layer thickness of alginate is much smaller compared to the salt), we can use the cross-sectional species mass to estimate the outer diameter of the combined alginate and gelled region (the fiber) using

$$R_g(z,t) = \left(\frac{M_1(z,t) + M_3(z,t)}{\pi C_{10}}\right)^{1/2} \tag{26}$$

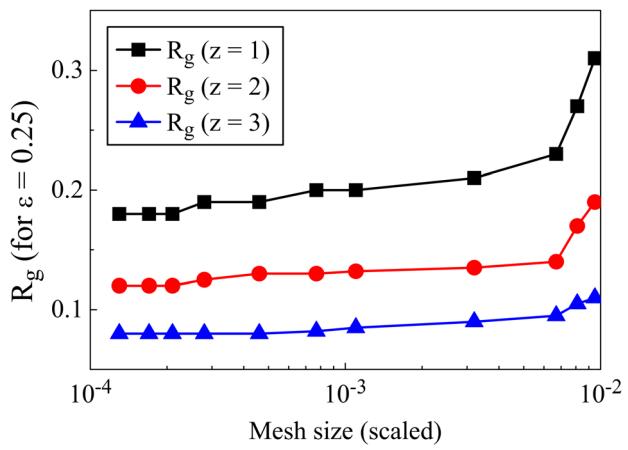


**Fig. 8 For the immiscible model, a study illustrating the impact of mesh size on the fiber radius $R_g$ at three downstream locations $z = 1$, 2, and 3**

In Fig. 8(*b*), we present the radii computed by Eq. (26) for each of the $\varepsilon$ and $\alpha$ values. For comparison, we also plot the nozzle inner radius, $r = R_0$. We see here that, in the fast core regime ($\varepsilon = 0.25$), the fiber radius reaches an equilibrium value closer to the nozzle than the slow core regime ($\varepsilon = 4$). We also see that increasing $\alpha$ leads to a larger gel radius $R_g$; this is also observed in Fig. 4(*b*) looking at the center of the gel maximum.

**4.3 Comparison of Immiscible, Miscible, and Analytical Results.** Previous works [14–16] have commonly treated the gel as fixed width, moving with fixed velocity, or offered no insight into what controls the radius; therefore, let us examine through Fig. 2(*a*) factors which influence the gel radius. For the immiscible model, we have selected the high surface tension solution ($We = 0.2$). The most important observation here is that both models have the same trend for radius as a function of relative flow rates ($\varepsilon$). This demonstrates that the global momentum transfer is very similar in both models. Some key differences can be seen though.

First, in Fig. 2(*a*), the transition toward the final equilibrium radius happens rapidly at small $z$ in the miscible model compared to a slower transition in the immiscible model (Note: the dotted lines in Fig. 2(*a*) are the solid lines in Fig. 8(*b*)). In particular for the case of $\varepsilon = 4$, the change in the radius using miscible model is very rapid, reaching a fully developed feature by $z \approx 0.75$, whereas for the immiscible model, the radius gradually approaches a constant value toward the end of the computational domain. For $\varepsilon = 0.25$, the transition toward a constant radius follows a similar trend for both the miscible and immiscible models, occurring, respectively, by $z \approx 1.5$ and $z \approx 4$. Moreover, for the miscible model, the radius changes almost monotonically as $z$ increases, whereas for the immiscible model, the radius has a more complicated evolution, featuring a maximum value (at $z = 2.8$) in the case of $\varepsilon = 4$; this is probably due to the combined effect of the azimuthal and radial components of surface tension.

In Fig. 2(*b*), looking at the axial velocity along $r = 0$, we show results consistent with the changes in alginate-gel radius. In particular, looking at the relative difference between the miscible and immiscible models for $\varepsilon = 4$, we see that using the immiscible model the velocity as $z \to 5$ is smaller, which is consistent with larger fiber radius as seen in Fig. 2(*a*).

Similar behavior is observed for the case $\varepsilon = 0.25$. In the nozzle region, we see the transition from shear pipe flow to core plug flow begins inside the nozzle, at $z \approx 0.5$ for both models. Contrasting Figs. 2(*a*) and 2(*b*), the differences between the immiscible and miscible models persist as we approach the end of the computational domain ($z = 5$).

From the above observations, an interesting question concerns whether the flow becomes fully developed. To establish this, we compare with the steady-state model described in Sec. 2.3.1. In Fig. 2(*c*), we show a comparison of the axial velocity plotted as a function of radius at $z = 4$ from all three models. The most important observation is that for $\varepsilon = 4$, there is general agreement between all three models. Comparing this to the results with $\varepsilon = 0.25$ (where results from both the miscible and immiscible models agree), but the steady-state model does not. Solving on a longer axial domain to allow for convergence to the fully developed flow profile for $\varepsilon = 0.25$ results in a flow profile which is in a much better agreement with the analytic solution for the velocity, as seen in Fig. 10 in Appendix D. In contrast, for $\varepsilon = 4$, the flow approaches the fully developed state rapidly compared to the length scale used for these simulations, but not for small $\varepsilon$. This is because the core flow is being compressed axially and not stretched.

We note at this point that the immiscible model includes a surface tension which contributes additional hydrodynamic pressure due to the azimuthal curvature, which is one of the reasons behind the discrepancy. We can conclude here that for the fast core regime $\varepsilon \gg 1$, the far-field analytical approximation can provide reasonably accurate estimation.

In thinking about the transition to a fully developed state, we look back at Fig. 4(*b*) and note that when $\varepsilon$ is small, the impact of increasing $\alpha$ is to exert a larger stress on the gel region, and hence, reduce the gradient of axial velocity in the core. This says that for the slow core regime, the flow development length increases with the reaction strength $\alpha$.

In Fig. 2(*d*), we show the axial dependence of the mass of gel and compare it to the value predicted by the simplified analytical model (Eq. (25)); note the dotted lines in Fig. 2(*d*) are the solid lines in Fig. 8(*a*). Here, $\delta$ in Eq. (25) is determined by matching to the miscible model case of $\varepsilon = 4$ to be $\delta \approx 16.5/\text{Pe}$. This value is then used for the other two comparisons on the graph. The main trend is that more gel is produced by increasing the core flow relative to the annular flow. However, in the slow core regime, we see from Fig. 8(*b*) that increasing $\alpha$ also produces more gel by axially slowing the flow and increasing its area. In contrast with the fast core regime, the impact of $\alpha$ is less significant.

## 5 Discussion

Herein, we have presented a fluid mechanics-based modeling study of the emerging cross-linking formation of solid calcium-alginate fiber from two miscible liquids. There are many other works on fiber formation; for example, those related to melt-spinning [1,2]; however, these works do not appear to involve the creation of an emerging interface which represents the fiber.

In the previous investigation of Bonhomme et al. [14], experimental observation of the fiber state (Table 1 and Fig. 3 in Ref. [14]) was tied to an estimate of shear stress based on the difference in mean flow rates $\sigma_e$ (Eq. (20) therein). In the limit of large difference, we can link $\varepsilon < 1$ in our model to $\sigma_e < 0$ in their model, and similarly, we link $\varepsilon > 1$ to $\sigma_e > 0$. Additionally, as noted in Sec. 2.3.2, their gel link density $\rho_{\text{link}}(z)$ (Eq. (19) therein) is our gel mass $M_3(z, t)$ normalized by the cross section area of gel and alginate (not gel). We present a significant step forward from Bonhomme by contrasting methods which can be used for computing the shear stress on the forming gel. Specifically, we have four general advancements. Primarily, as captured in Figs. 6(*a*)–6(*c*), our analysis is applicable to arbitrarily shaped nozzles and junctions of which there are a diverse range in earlier works, this will aid more direct comparison with experiments (including Bonhomme and others investigators in this field). Then, subsequently as captured by Figs. 2(*a*), 5, and 8(*b*), the gel is not of fixed shape; the gel width is affected by gelation; finally, we have outlined how observations of gel shape might be related to whether the gel behaves as a surface-tension or a viscous effect.

From an alternative perspective, our advancements are that we do not fix the velocity field (assumed by Bonhomme et al. [14] and Li et al. [16]) and that we have two-way coupled the hydrodynamics to the chemistry [15,16]. Additionally, none of these previous works examined the detailed flow field around the nozzle. By modeling the fluid motion around the nozzle, prior to the fluids meeting, we are able to consider the impact of the hydrodynamics on the alginate formation as it exits the nozzle. Also, we treat the emerging interface as an outcome of the chemical reaction in the miscible model; this eliminates the need to prescribe where it begins. Assuming the no-slip law fully applies for the polymer alginate solution (discussed later), we have a rapid transition from shear-flow to plug-flow at the nozzle, which drives rapid changes in alginate shape. In the nozzle, the alginate is sheared, while outside the nozzle, it is in plug flow, and lubricated by the annular flow. Herein, we have presented two numerical models which fully couple the representation of the gel to fluid motion, in addition to contrasting with fully developed flow conditions. Although in the miscible model we have under-resolved the fiber thickness, the results we present are qualitatively correct.

In comparison of the miscible and immiscible models with the fully developed analytical flow model, we observed good agreement in the fast core flow, this is because the more mobile annular flow rapidly adjusts to the fully developed state. However, in the slow core flow, the axial flow develops much more slowly; for an experiment, the axial length and outflow conditions will be important conditions to determine the velocity profile observed (as discussed in Appendix D).

In the recent work, Li et al. [16] (Fig. 5(*i*), therein) investigated the formation of calcium alginate fibers with calcium solution in the nozzle and alginate in the annulus. Using higher viscosity alginate (3% w/v), they observe the rapid expansion of the alginate at the nozzle exit, which they ascribe purely to the formation of the gel. Based on our results here, we propose that this behavior is due to the pressure gradient in the strongly sheared alginate being much greater than that in their core calcium solution.

In our work, we have assumed that the motion of the alginate in the nozzle obeys the no-slip condition, whereas in certain instances polymer solutions can exhibit slip at a wall [24,25]. If this happens here, it would reduce the pressure gradients in the nozzle, consequently impacting changes to the fiber radius. Furthermore, we should note that imposing symmetry prevents us from exploring symmetry breaking modes, where the alginate fiber may buckle as external pressure on the fiber exceeds internal pressure, or wrinkle, which is beyond the scope of our present study, but also noted as an important factor in Ref. [14].

Once an application is defined, it would be important to understand common environmental factors such as the impact of pressure, temperature, and external chemistries. The work presented herein has been considered at standard temperature and pressure, and without the presence of other chemistries. A change in the chemical environment could reverse the cross-linking reaction effectively dissolving the fibers. In addition to impacting the cross-linking reaction, the mechanical and thermal stability of the formed fibers would be important variables to understand.

In this work, the cross-linked fiber has been treated as a very viscous liquid; we note experimental measurements by Cuadros et al. [26] detail the elastic properties of the formed calcium-alginate fibers; thus, depending on the application a model which captures the viscous and elastic regimes may be relevant. Future studies of this problem might focus on the use of a more sophisticated approach to resolve the fiber interface near the nozzle along the lines of the immiscible model and the dynamics with higher concentration solutions.

## 6 Conclusion

Alginate fibers are formed by the cross-linking reaction of aqueous polymer chains with a salt solution; in a flowing system, continuous gel fibers may be formed. We have presented two alternative models of flowing gel fiber formation; these are significant advancements on previous works [14–16] for several reasons. First, as per Figs. 2(*a*), 5, and 8(*b*), we compute the gel fiber radius rather than assuming it as a fixed value. We observe significant changes in the fiber radius. Second, we two-way couple the chemistry to the hydrodynamics, this allows us to investigate how the chemistry controls the hydrodynamics. We observe that chemistry changes gel stresses, and hence, the gel radius and mass (as shown in Fig. 8(*b*)). Third, we contrast the representations of the emerging gel fiber as a surface-tension or chemistry-driven-viscous effect. This demonstrates the need for observations at the nozzle to confirm the gel shape. Fourth, we provide a characterized framework for future works to examine alternative gel representation, and explore the precise role of elongational stress and symmetry identified in Ref. [14]. In our two models, the fiber radius and the morphology of the forming gel and their governing mechanisms have been thoroughly explored. Our results present significant improvements on the fixed-domain one-way coupled models in the previous literature works. Our work is an important step toward understanding factors which influence the fabrication of the flowing cross-linked gel in particular the mass and radius.

A key objective of the work was to explore the two-way coupling between the hydrodynamics and the chemistry using the miscible fluid model which captures the gel by making the

viscosity of the solution depend on the gel concentration. A regime in which this coupling is particularly important is the slow core flow, which is accelerated by the outer annular flow. Here, the formation of the gel causes the core flow to slowdown relative to the situation where the viscosity is unaffected by the species concentration. This accounts for the cross-sectional expansion of the core and increase in the mass of gel produced. Features of this solution to be explored in future work include the impact of azimuthal gel strength versus axial gel strength and the likelihood of nonaxisymmetric buckling in the gel structure. In the fast core regime, where the core flow is faster than the annular flow, the alginate-fiber is compressed, and the cross-linking has a smaller impact on the hydrodynamics; this may be due to the role of azimuthal stresses. In solving the miscible model, we did not fully resolve the Peclet number boundary layer, but qualitative behavior of the systems appears to be independent of this.

When we represent the gel as an interface using the stress balanced by the surface-tension in the immiscible fluid model, we observe a shape near the co-axial nozzle that is different from results obtained by the miscible model where the gel layer has the viscous effect without any surface tension. The interface shape changed more slowly compared to the viscous model. Neither of these conclusions could be examined with earlier models in the literature. However, far downstream of the nozzle, both the miscible and immiscible models lead to the same trend in the fiber radius as a function of $\varepsilon$.

The work presented here has provided an intermediate step in how to model an emerging interface which changes from mobile fluid to a nearly immobile solid at a junction. In particular, we have demonstrated methods which could be used for evaluating the stress field near the gel formation. This approach can be generalized to other geometrical setups. Next steps could include combining the viscous and surface-tension phenomena; the use of a concentration dependent shear-thinning rheology with a visco-elastic model; understanding the azimuthal physics and importance of symmetry as noted by Bonhomme. Additionally, we should explore behavior in higher concentration alginate, typically used in experiments.


## Acknowledgment

The authors would like to gratefully thank the following people for their insight and help at various stages in this work: Phil Sullivan, Brent Busby, and Giselle Refunjol at Schlumberger; David Baker at University of Cambridge and Colin Peter Please at University of Oxford. This work was funded through Schlumberger Gould Research and University of Oxford (EPSRC CDT programme). Sourav Mondal is thankful to the Royal Society for funding his position at University of Oxford via EPSRC EP/N005147/1.

## Funding Data

- Engineering and Physical Sciences Research Council (EP/L015803/1).
- University of Oxford (EP/N0051471/1).


## Nomenclature

$A_1$ = nondimensional nozzle cross-sectional area
$A_2$ = nondimensional annulus cross-sectional area
$b_d$ = nondimensional coefficient for the alginate viscosity function of concentration
$C_i$ = nondimensional concentration of species $i = 1$ (alginate), 2 (salt), and 3 (gel)
$C_{10}^*$ = alginate concentration at nozzle inlet and initial condition
$C_{20}^*$ = salt concentration at annulus inlet and initial condition
Ca = capillary number
$D_i^*$ = diffusion coefficient of species $i$
$\underline{e}_r$ = radial basis vector
$\underline{e}_z$ = axial basis vector
$\mathbf{F}$ = axisymmetric body force per unit volume
$G$ = total axial flux of gel
$\mathbf{I}$ = identity tensor
$m$ = nondimensional parameter in Carreau–Yasuda law
$M_i$ = cross-sectional mass of species $i$
$\mathbf{n}$ = outward normal vector
$N_c$ = nondimensional stoichiometric coefficient for cross-linking
$N_{\text{phase}}$ = number of phases
$p$ = nondimensional pressure
Pe = Peclet number
$Q_1$ = nondimensional volumetric flow rate into nozzle
$Q_2$ = nondimensional volumetric flow rate into annulus
$r$ = nondimensional radial distance
$R_g$ = fiber gel radius
$R_m$ = intermediate variable in initial conditions
$R_0$ = nondimensional radial distance to nozzle inner wall
$R_1$ = nondimensional radial distance to nozzle outer wall
$R^*$ = dimensional outer pipe radius
Re = Reynolds number
$S_i^*$ = reaction rate of species $i$
$t$ = nondimensional time
$\boldsymbol{T}$ = nondimensional total stress tensor in the fluid
$u$ = nondimensional radial component of velocity
$\mathbf{u}$ = axisymmetric velocity vector
$w$ = nondimensional axial component of velocity
$w_1$ = core fluid velocity
$w_2$ = annular fluid velocity
$w_s^*$ = axial velocity scale
We = Weber number
$z$ = nondimensional axial distance
$z_0$ = axial distance downstream
$\beta_i$ = phase volume fraction
$\beta_r$ = reaction scale
$\dot{\gamma}$ = nondimensional shear-rate
$\dot{\boldsymbol{\gamma}}$ = Rate of strain tensor
$\delta$ = length-scale of salt depleted region surrounding alginate/gel core
$\varepsilon$ = ratio of mean nozzle and annular inflow velocities
$\eta$ = intermediate variable in computation of reaction rate
$\Theta_i$ = scaled diffusivity
$\kappa_i$ = interface curvature
$\kappa_r^*$ = dimensional rate coefficient of formation of alginate dimer
$\lambda$ = nondimensional parameter in Carreau–Yasuda law
$\mu$ = nondimensional dynamic fluid viscosity
$\mu_p$ = nondimensional zero shear-rate viscosity
$\mu_1$ = core fluid viscosity
$\mu_2$ = annular fluid viscosity
$\mu_2^*$ = dimensional viscosity of salt solution (viscosity scale)
$v_b^*$ = dimensional mean inflow velocity
$\rho^*$ = dimensional fluid density
$\sigma_{12}^*$ = surface tension scale (surface tensions between fluids 1 and 2)

## Appendix A: Grid Refinement

For the miscible model, in Fig. 9, we show how the solutions behave under adaptive grid refinement for the case $\alpha = 0$ and $\varepsilon = 1$. We annotate solutions by the number of successive level of refinement, which were computed based on the gradient of gel concentration. At each level of refinement, the number of elements on the domain is increased by about 70%. Level 0 is the default resolution as detailed in Sec. 3.2, used for all other miscible model simulations presented in this paper. In Fig. 9(*c*), we see that the width of the gelled region appears to converge, whereas the maximum value of the gel concentration does not converge.

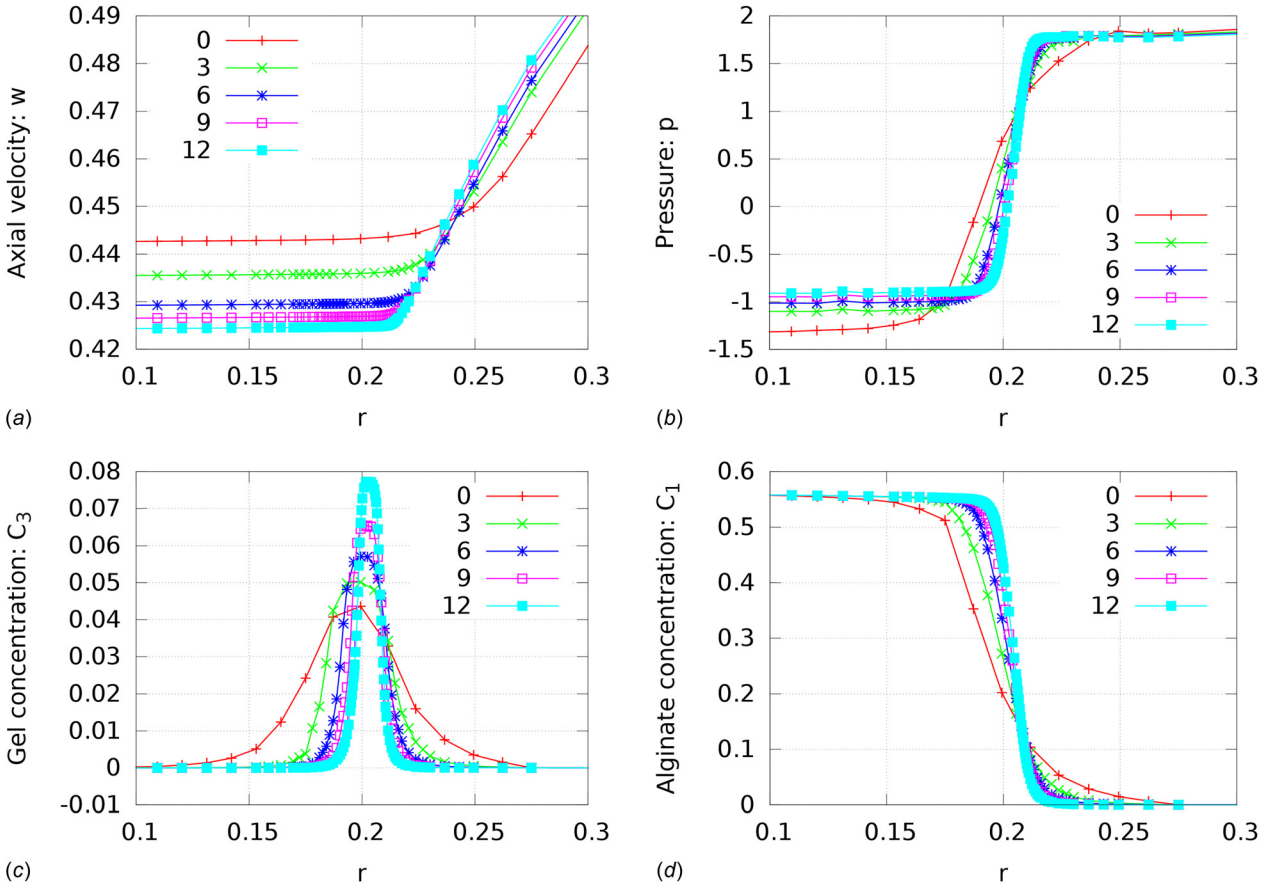


**Fig. 9 For the miscible model, graphs of adaptively refined mesh solutions with $\varepsilon = 1$, $\alpha = 0$. The number in the key refers to the number of levels of refinement based on resolving the concentration gradient adequately.**

However, while the gel concentration suffers convergence issues, the qualitative nature of the axial flow field does not change. Figures 9(*b*) and 9(*d*) demonstrate respectfully that the pressure field converges very well as does the alginate concentration. The solutions shown here are from a $z = 2$ slice and were computed on a smaller computational domain of length $z = 2.5$, half that used in the results presented in the rest of the paper. The conclusion is that while we under-resolve the Peclet number boundary layer, the qualitative features of the flow are correctly captured. Ultimately, achieving convergence may require a more flexible solver than that used herein.

## Appendix B: Estimating Rate of Gel Formation

To understand the rate of gel formation, let us assume no radial flow and look at the mass transfer of each chemical species as described by the quasi-steady advection-diffusion-reaction equation in dimensionless form

$$w_i \frac{\partial C_i}{\partial z} = \Theta_i \nabla^2 C_i + S_i \tag{B1}$$

where $\Theta_i = \{0.1/\mathrm{Pe}, 1/\mathrm{Pe}, 0\}$ for the alginate, salt, and gel, respectively, and $w_i$ is the average fluid velocity for the respective species. Integrating the advection-diffusion-reaction equation for the salt over the radius of the pipe gives

$$\int_0^1 w_2 \frac{\partial C_2}{\partial z} r \mathrm{d}r = \int_0^1 (\Theta_2 \nabla^2 C_2 + S_2) r \mathrm{d}r \tag{B2}$$

The salt sink ($S_2$) depends on the concentration of all three species. If the diffusivity of alginate is taken as approximately zero (it is an order of magnitude smaller than that of the salt), the alginate is localized to the fluid streak lines. Now we are left to consider the diffusion of calcium into some alginate/fiber of radius, say, $R_g$ (where $R_g R^*$ is the dimensional gel fiber radius). Outside the fiber, the sink term will be zero, and on the inside, the sink term will be large, i.e., we assume

$$\forall r < R_g, \quad S_2 \gg \Theta_2 \nabla^2 C_2 \tag{B3}$$

$$\forall r > R_g, \quad S_2 \ll \Theta_2 \nabla^2 C_2 \tag{B4}$$

so the integral on the right-hand side of Eq. (B2) can be split into two parts as

$$\int_0^1 w_2 \frac{\partial C_2}{\partial z} r \mathrm{d}r \approx \int_0^{R_g} (S_2) r \mathrm{d}r + \int_{R_g}^1 (\Theta_2 \nabla^2 C_2) r \mathrm{d}r \tag{B5}$$

We are not interested in the contributions of diffusion in the $z$ direction due to the lubrication approximation as the flow has a large aspect ratio. The rate of salt consumption can be replaced by the rate of gel production using the stoichiometry relations given in Eq. (14). Incorporating these insights leads us to

$$\bar{w}_2 \frac{\partial}{\partial z} \int_0^1 C_2 r \mathrm{d}r \approx \int_0^{R_g} -N_c S_3 r \mathrm{d}r + \int_{R_g}^1 \Theta_2 \frac{\partial}{\partial r} \left( r \frac{\partial C_2}{\partial r} \right) \mathrm{d}r \tag{B6}$$

$$\bar{w}_2 \frac{\partial M_2}{\partial z} \approx \int_0^{R_g} -N_c w_1 \left( \frac{\partial C_3}{\partial z} \right) r \mathrm{d}r + \left[ \Theta_2 r \frac{\partial C_2}{\partial r} \right]_{R_g}^1 \tag{B7}$$

$$\bar{w}_2 \frac{\partial M_2}{\partial z} \approx -w_1 N_c \frac{\partial}{\partial z} \int_0^{R_g} C_3 r \mathrm{d}r - \Theta_2 R_g \frac{\partial C_2(R_g, z)}{\partial r} \tag{B8}$$

$$\bar{w}_2 \frac{\partial M_2}{\partial z} \approx -w_1 N_c \frac{\partial M_3}{\partial z} - \Theta_2 R_g \frac{\partial C_2(R_g, z)}{\partial r} \tag{B9}$$

where $M_i$ is the total mass of species $i$ at some downstream distance $z$, and we have specified no flux at the pipe wall (18). If we have a lot of salt in the annular solution such that $M_2 \gg M_3$, we must satisfy

$$w_2 \frac{\partial M_2}{\partial z} \approx 0 \tag{B10}$$

which implies that the mass of gel term balances with the flux of salt term

$$w_1 N_c \frac{\partial M_3}{\partial z} \approx -\Theta_2 R_g \frac{\partial C_2(R_g, z)}{\partial r} \tag{B11}$$

So, the mass of gel in a cross-sectional region of the pipe changes in the downstream as

$$\frac{\partial M_3}{\partial z} \approx -\frac{R_g \Theta_2}{N_c w_1} \frac{\partial C_2(R_g, z)}{\partial r} \tag{B12}$$

The flux ($Q$) across the surface of cylinder of radius $r$ can be described by Ficks first law of diffusion as

$$Q = -r \frac{\partial C_2(r, z)}{\partial r} \tag{B13}$$

So, integrating Eq. (B13) between $(R_g - \delta, R_g + \delta)$ for $\Theta \ll \delta \ll 1$ leads to

$$\int_{R_g-\delta}^{R_g+\delta} \frac{Q}{r} \mathrm{d}r = -\int_{C_2(R_g-\delta)}^{C_2(R_g+\delta)} \mathrm{d}C_2 \tag{B14}$$

$$Q \log\left(\frac{R_g + \delta}{R_g - \delta}\right) = C_2(R_g - \delta) - C_2(R_g + \delta) \tag{B15}$$

Considering the Taylor series expansion of the logarithmic term in Eq. (B15)

$$\log\left(\frac{R_g + \delta}{R_g - \delta}\right) \approx \left(\frac{R_g + \delta}{R_g - \delta} - 1\right) + \mathcal{O}\left(\left(\frac{R_g + \delta}{R_g - \delta} - 1\right)^2\right) \tag{B16}$$

$$\approx \frac{2\delta}{R_g} + \mathcal{O}\left(\left(\frac{2\delta}{R_g}\right)^2\right) \tag{B17}$$

We also know that inside the alginate/gel layer, the calcium concentration is small (as it is consumed so rapidly), and outside the alginate/gel layer, it is approximately unchanged (as $\Theta_2$ is small). This leads to the approximation that $\delta$ is constant for a particular setup; it can be determined by fitting one set of data, providing a good approximation for other flow rates used in this setup. Therefore, the right-hand side of Eq. (B15) can approximated by the initial (bulk) concentration of salt in the annular fluid ($C_{20}$). The flux of calcium into the alginate/gel sleeve is then represented by

$$Q \approx \frac{C_{20} R_g}{2\delta} \tag{B18}$$

which, when included in Eq. (B12), gives

$$\frac{\partial M_3}{\partial z} \approx \frac{R_g \Theta_2 C_{20}}{2 N_c w_1 \delta} \tag{B19}$$

## Appendix C: Solution Method for the Immiscible Fluid Interface Model

In the standard CSF method formulation, the curvature of the interface ($\kappa_i$) is defined by divergence of the normalized gradient of the phase volume fraction $\beta_i$ as

$$\kappa_i = \nabla \cdot \frac{\nabla \beta_i}{|\nabla \beta_i|} \tag{C1}$$

Here, $\kappa_i$ is not to be confused with $\kappa_r^*$, which denote reaction rates used in other sections; similarly, $\beta_i$ is not to be confused with $\beta_r$, which denotes reaction scale in other sections. The tracking of the interface(s) between the phases is accomplished by the solution of a continuity equation for the volume fraction of one (or more) of the phases. Since $\beta_i$ is a scalar function which is always equal to zero at any point on the fluid interface, its material derivative at any location on the interface is obviously equal to zero (assuming that there is no phase or mass transfer across the interface)

$$\frac{1}{\rho_i}\left(\frac{\partial}{\partial t}(\beta_i \rho_i) + \mathbf{u} \cdot \nabla \rho_i \beta_i\right) = 0 \tag{C2}$$

$$\sum_{i=1}^{N_{\text{phase}}} \beta_i = 1 \tag{C3}$$

where $N_{\text{phase}}$ is the number of phases in the system (equals 2 in this case) and $\rho_i$ is the density of component $i$. The initial conditions for the phase variables (assuming a flat interface at $r = R_0 \, \forall z$) are

$$\beta_1(0 \le r \le R_0, z, 0) = 1, \quad \beta_2(R_0 \le r \le 1, z, 0) = 0 \tag{C4}$$

and the boundary conditions ($z = 0$) as

$$\beta_1(0 \le r \le R_0, 0, t) = 1, \quad \beta_2(R_1 \le r \le 1, 0, t) = 1 \tag{C5}$$

The effects of the surface tension forces at the interface are integrated into the system through an additional body term in Eq. (2) as a function of the phase volume fraction $\beta_i$

$$\mathbf{F} = \sum_{\text{pairs}}^{N_{\text{phase}}} \sum_{ij, i<j} 2\sigma_{ij} \frac{\text{Re}}{\text{We}} \frac{\beta_i \rho_i \kappa_j \nabla \beta_j + \beta_j \rho_j \kappa_i \nabla \beta_i}{(\rho_i + \rho_j)} \tag{C6}$$

where Weber number $\text{We} = \rho^* w_s^{*2} R^* / \sigma_{12}^*$. In the case of two phases $\kappa_1 = -\kappa_2$ and $\nabla \beta_1 = -\nabla \beta_2$, with similar density ratios $(\frac{\rho_1}{\rho_2} \approx 1)$, Eq. (C6) can be simplified as

$$\mathbf{F} = \frac{\text{Re}}{\text{We}} \kappa_1 \nabla \beta_1 \tag{C7}$$

In this model formulation, the zero-shear viscosity ($\mu_p$) in Eq. (6) is related to the alginate concentration $C_2$ (in phase 1) as $\mu_p = 1 + b_d C_2$ and for the salt solution (phase 2) $\mu_p = 1$. The variables $C_2$, $b_d$, etc., are defined in Sec. 2.3. The VOF model solves a single set of momentum equation (Eqs. (2)–(6)) based on the volume averaged mixture quantities. However, the phase continuity equations are solved for the individual phases ($N_{\text{phase}} - 1$ equations are solved for $N_{\text{phase}}$ number of phases). From a scaling analysis, the primary dimensionless parameters are Weber number (We) or capillary number (Ca), and Reynolds number (Re) which govern the physical processes. In the case, when the viscous force is dominant ($\text{Re} < 1$), Capillary number ($\text{Ca} = \mu_2^* w_s^* / \sigma_{12}^*$) is relevant, and in the case of strong advection ($\text{Re} \gg 1$), Weber number is important ($\text{We} = \text{Re} \cdot \text{Ca} = \rho^* w_s^{*2} R^* / \sigma_{12}^*$).

## Appendix D: Developing Velocity Profile for Small ε

In order to understand the underlying physics behind the discrepancy with the analytical result in the far-field for small core flows ($\varepsilon < 1$) in Fig. 2(*c*), we have calculated the solution (for the

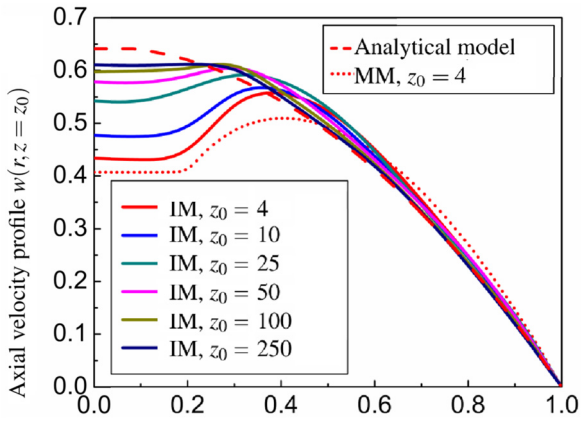


**Fig. 10 Comparison of the developing velocity profile obtained from the immiscible model (IM) with increasing axial domain for $\varepsilon = 0.25$. The results with the miscible model (MM) are for $\alpha = 100$.**

immiscible case in this situation) in a much longer domain than presented in Fig. 2(*c*) ($z \gg 5$). In Fig. 10, the variable $z_0$ defines the downstream location at which the radial velocity profile is computed. The results show the developing nature of the hydrodynamic profile. The developing region is larger on reducing the core flow ($\varepsilon < 1$), as expected. It is now evident that the computational velocity further away in the downstream is close to the far field approximation ($z \to \infty$) in the analytical model. We expect similar qualitative trends would emerge from a longer domain simulation of the miscible model. However, we have not done that, as it is too computationally intensive solving an additional coupled scalar transport equation together with the fluid flow.

## Appendix E: Advective Mass Balance

To demonstrate the total mass of alginate and gel is conserved in the model, let us examine the combined axial flux $G$ of alginate and gel using

$$G(z,t) = (M_1(z,t) + M_3(z,t))w_1(0,z,t)/(Q_1C_{10}) \tag{E1}$$

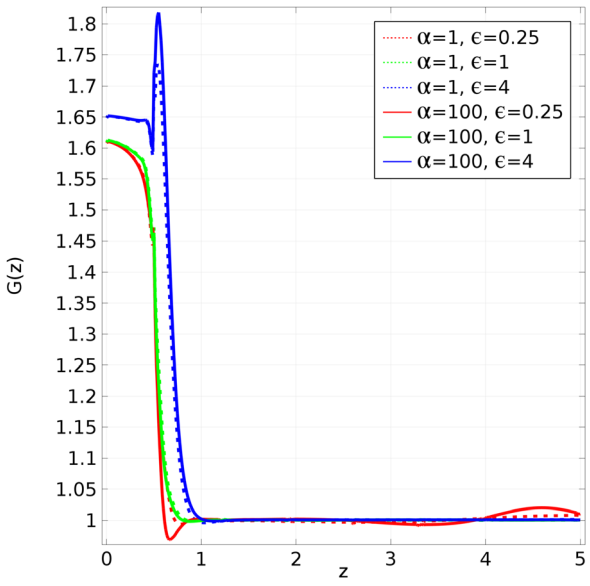


**Fig. 11 Here, we show the impact of varying $\alpha = 1$ and 100 and $\varepsilon = 0.25$, 1, and 4 on the total axial flux of gel $G$ (Eq. (E1))**

where $Q_1C_{10}$ is the flux of alginate through the nozzle, as specified in Eqs. (7) and (16).

Here, the flux is rescaled by the initial value of gel and alginate at the nozzle inlet: $Q_1C_{20}$, so it approaches a uniform value in the downstream, as depicted in Fig. 11. On the upstream of the nozzle, the velocity $w(0, z)$ is the peak velocity (and not the mean velocity) which approaches $(\text{peak velocity})/(\text{mean velocity}) \approx 2.35/(\varepsilon/(\pi(1 - R_1^2))) \approx 1.65$ for $\varepsilon = 4$ and $\approx 1.6$ for $\varepsilon = 1$, 0.25. The axial flux varies most notably close to the nozzle exit which ultimately reduces in the downstream. Although there are overshoots here, all the components of the flux ($w(0, z)$, $M_1(z)$, and $M_3(z)$) vary smoothly. Overall, this result gives us confidence on the numerical computation that as one moves away from the nozzle, having an under-resolved Peclet number boundary layer, the approximation is accurate in terms of the axial advection. This result also demonstrates that the total mass of alginate (and hence gel) is conserved in the model.

## References


[1] Park, C.-W., 1990, "Extensional Flow of a Two-Phase Fiber," AIChE J., **36**(2), pp. 197–206.

[2] Lipscomb, G. G., 1994, "The Melt Hollow Fiber Spinning Process: Steady-State Behavior, Sensitivity and Stability," Polym. Adv. Technol., **5**(11), pp. 745–758.

[3] Barge, L. M., Cardoso, S. S., Cartwright, J. H., Cooper, G. J., Cronin, L., De Wit, A., Doloboff, I. J., Escribano, B., Goldstein, R. E., Haudin, F., Jones, D. E. H., Mackay, A. L., Maselko, J., Pagano, J. J., Pantaleone, J., Russell, M. J., Ignacio Sainz-Diaz, C., Steinbock, O., Stone, D. A., Tanimoto, Y., and Thomas, N. L., 2015, "From Chemical Gardens to Chemobrionics," Chem. Rev., **115**(16), pp. 8652–8703.

[4] Mikkelsen, A., and Elgsaeter, A., 1995, "Density Distribution of Calcium-Induced Alginate Gels—A Numerical Study," Biopolymers, **36**(1), pp. 17–41.

[5] Braschler, T., Valero, A., Colella, L., Pataky, K., Brugger, J., and Renaud, P., 2011, "Link Between Alginate Reaction Front Propagation and General Reaction Diffusion Theory," Anal. Chem., **83**(6), pp. 2234–2242.

[6] Thumbs, J., and Kohler, H.-H., 1996, "Capillaries in Alginate Gel as an Example of Dissipative Structure Formation," Chem. Phys., **208**(1), pp. 9–24.

[7] Treml, H., and Kohler, H.-H., 2000, "Coupling of Diffusion and Reaction in the Process of Capillary Formation in Alginate Gel," Chem. Phys., **252**(1–2), pp. 199–208.

[8] Treml, H., Woelki, S., and Kohler, H.-H., 2003, "Theory of Capillary Formation in Alginate Gels," Chem. Phys., **293**(3), pp. 341–353.

[9] Secchi, E., Roversi, T., Buzzaccaro, S., Piazza, L., and Piazza, R., 2013, "Biopolymer Gels With "Physical" Cross-Links: Gelation Kinetics, Aging, Heterogeneous Dynamics, and Macroscopic Mechanical Properties," Soft Matter, **9**(15), pp. 3931–3944.

[10] Wu, Z. L., Takahashi, R., Sawada, D., Arifuzzaman, M., Nakajima, T., Kurokawa, T., Hu, J., and Gong, J. P., 2014, "In Situ Observation of $Ca^{2+}$ Diffusion-Induced Superstructure Formation of a Rigid Polyanion," Macromolecules, **47**(20), pp. 7208–7214.

[11] Vempati, B., Panchagnula, M. V., Öztekin, A., and Neti, S., 2007, "Numerical Investigation of Liquid-Liquid Coaxial Flows," ASME J. Fluids Eng., **129**(6), pp. 713–719.

[12] Govindarajan, R., and Sahu, K. C., 2014, "Instabilities in Viscosity-Stratified Flow," Annu. Rev. Fluid Mech., **46**(1), pp. 331–353.

[13] Shin, S.-J., Park, J.-Y., Lee, J.-Y., Park, H., Park, Y.-D., Lee, K.-B., Whang, C.-M., and Lee, S.-H., 2007, "On the Fly" Continuous Generation of Alginate Fibers Using a Microfluidic Device," Langmuir, **23**(17), pp. 9104–9108.

[14] Bonhomme, O., Leng, J., and Colin, A., 2012, "Microfluidic Wet-Spinning of Alginate Microfibers: A Theoretical Analysis of Fiber Formation," Soft Matter, **8**(41), pp. 10641–10649.

[15] Li, S., Liu, Y., Li, Y., Zhang, Y., and Hu, Q., 2015, "Computational and Experimental Investigations of the Mechanisms Used by Coaxial Fluids to Fabricate Hollow Hydrogel Fibers," Chem. Eng. Process., **95**, pp. 98–104.

[16] Li, Y., Liu, Y., Jiang, C., Li, S., Liang, G., and Hu, Q., 2016, "A Reactor-Like Spinneret Used in 3D Printing Alginate Hollow Fiber: A Numerical Study of Morphological Evolution," Soft Matter, **12**(8), pp. 2392–2399.

[17] Leal, L., 2007, "Advanced Transport Phenomena: Fluid Mechanics and Convective Transport Processes," *Cambridge Series in Chemical Engineering*, Cambridge University Press, Cambridge, UK.

[18] Leonard, B. P., 1979, "A Stable and Accurate Convective Modelling Procedure Based on Quadratic Upstream Interpolation," Comput. Methods Appl. Mech. Eng., **19**(1), pp. 59–98.

[19] Youngs, D. L., 1982, "Time-Dependent Multi-Material Flow With Large Fluid Distortion," Numer. Methods Fluid Dyn., **24**(2), pp. 273–285.

[20] Issa, R. I., 1986, "Solution of the Implicitly Discretised Fluid Flow Equations by Operator-Splitting," J. Comput. Phys., **62**(1), pp. 40–65.

[21] Patankar, S., 1980, *Numerical Heat Transfer and Fluid Flow*, CRC Press, Boca Raton, FL.
[22] Bonhomme, O., 2011, "étude de la formation de fibres en microfluidique: Compétition entre mise en forme et gélification de fluides complexes sous écoulement," Ph.D. thesis, l'université Bordeaux-I, Bordeaux, France.
[23] Graham, M. D., 2003, "Interfacial Hoop Stress and Instability of Viscoelastic Free Surface Flows," Phys. Fluids, **15**(6), pp. 1702–1710.
[24] Cohen, Y., and Metzner, A., 1985, "Apparent Slip Flow of Polymer Solutions," J. Rheol., **29**(1), pp. 67–102.
[25] Denn, M. M., 2001, "Extrusion Instabilities and Wall Slip," Annu. Rev. Fluid Mech., **33**(1), pp. 265–287.
[26] Cuadros, T., Skurtys, O., and Aguilera, J., 2012, "Mechanical Properties of Calcium Alginate Fibers Produced With a Microfluidic Device," Carbohydr. Polym., **89**(4), pp. 1198–1206.